Electronic Supplementary Material (ESI) for Nanoscale.
This journal is © The Royal Society of Chemistry 2023

Supplementary information

# Nanoscale insights into local structural rearrangements of amyloid-β induced by bexarotene

Kamila Sofińska[a], Piotr Batys[b], Adrian Cernescu[c], Dhiman Ghosh[d], Katarzyna Skirlińska-Nosek[a,e], Jakub Barbasz[b], Sara Seweryn[a,e], Natalia Wilkosz[a], Roland Riek[d], Marek Szymoński[a], Ewelina Lipiec[*a]

[a] Jagiellonian University, Faculty of Physics, Astronomy and Applied Computer Science, M. Smoluchowski Institute of Physics, Łojasiewicza 11, 30-348 Krakow, Poland

[b] Jerzy Haber Institute of Catalysis and Surface Chemistry, Polish Academy of Sciences, Niezapominajek 8, 30-239 Krakow, Poland

[c] Attocube Systems AG, Eglfinger Weg 2, 85540 Haar, Germany

[d] ETH Zürich, Laboratory of Physical Chemistry, 8093 Zürich, Switzerland

[e] Jagiellonian University, Doctoral School of Exact and Natural Sciences, Krakow, Poland

[*]E-mail: ewelina.lipiec@uj.edu.pl

**Table of Contents**

## Experimental Procedures

### Recombinant peptide preparation protocol

For $A\beta_{(1-42)}$ the DNA construct was cloned for the expression of the protein sequence $(NANP)_{19}$-RSM-DAEFRHDSGYEVHHQKLVFFAEDVGSNKG-AIIGLLVGGVVIA into the pRSETA-Vector (Invitrogen) using the BamHI and EcoRI restriction sites. The substitution of MET35 by LEU was introduced allowing the separation of the $^{35L}Ab_{(1–42)}$ peptide from the N-terminal fusion peptide by cyanogen bromide cleavage.

The expression was performed in *Escherichia coli* (BL21(DE3)). The cells were induced at an $OD_{600}$ *1.3 at 37 °C for 12 h. The protein containing a N-terminal hexahistidine tag was purified by a Nickel-NTA agarose column and further by reversed-phase chromatography (RPC). The cleavage was subsequently performed with tobacco etch virus (TEV) protease in order to obtain the correct sequence of $A\beta_{(1–42).}$ Furthermore, the peptide was purified using previously established protocols.[1,2] Several biophysical techniques such as Ni-chromatography followed by HPLC to purify $A\beta_{(1-42)}$ were applied. Immediately after elution of $A\beta_{(1-42)}$ in a monomeric form from HPLC, it was lyophilized and stored at -200 °C until further use.

### Amyloid beta aggregation protocol

In the first step, lyophilized amyloid-β was suspended in a freshly prepared phosphate buffer (pH 7.4) to a concentration of 30 µM. The pH of the solution was then adjusted to c.a. 10 with NaOH, and sonicated for 2-3 minutes in an ice bath (using an ultrasonic homogenizer performing at 50–60% of maximum power). The pH of the solution was then adjusted to 7.4 with HCl. The resulting amyloid-β solution was filtered with a 0.22 µm syringe filter.

Then peptide solution was mixed with the stock solution of bexarotene (dissolved in DMSO) to obtain a final concentration of the drug of 10 µM, or 100 µM. Amyloid-β samples in the absence (control sample) or presence of aggregation inhibitor were incubated at 37 °C in the darkness.

The time between the beginning of the aggregation and AFM image collection/ATR-FTIR spectrum acquisition is in the range of a few minutes (transfer of the sample, deposition on mica for AFM/ evaporation of water for ATR-FTIR). Therefore, it should be taken into consideration that in spectra and images of samples referred to 0h time, oligomeric species and their spectral signature might be observed.

### Preparation of samples for AFM imaging

To prepare samples for AFM imaging, 10 µl of the $A\beta_{(1–42)}$ solution was deposited on a silicon support. After 15 minutes of incubation, the silicon wafer was rinsed with 1-2 ml of ultrapure water to remove the peptide excess, then dried under a gentle stream of compressed $N_2$.

### AFM imaging

AFM images were acquired in a tapping mode using Multimode AFM Nanoscope IIIa system (Digital Instrument, Santa Barbara, CA, USA) performing in air. We applied HA_NC ETALON cantilevers (NT-MDT Spectrum Instruments). 1x1 $um^2$ images were collected with a scan rate of 0.5 Hz, and an image resolution of 432x432 pixels. Processing of acquired AFM images relied on flattening by a 1st order polynomial correction using Gwydion software[3] (Version 2.51).

**ATR-FTIR spectroscopy**

ATR-FTIR spectra were acquired from dried droplets of amyloid solutions deposited directly on the diamond ATR window. Data was collected with 64 interferograms co-added, and 4 $cm^{-1}$ spectral resolution.

**Infrared nanospectroscopy**

Nano-FTIR spectra and mapping were performed using a commercial s-SNOM nanoscope device (NeaSNOM, Neaspec Attocube systems, Haar, Munich, Germany) operating in a tapping mode. Single point nano-FTIR spectra were collected with an IR broadband laser source (Toptica, Graefelfing, Munich, Germany) using an NCPt-Arrow AFM probes (Nanoworld AG). The resolution of nano-FTIR spectra was 10-12.5 $cm^{-1}$. Background spectra were acquired from a clean silicon wafer and used for normalization to remove the instrumental response. s-SNOM mapping was performed at 1630 $cm^{-1}$ and 1649 $cm^{-1}$ with a tunable QCL laser (Mircat, Daylight Solutions, Wausau, WI, USA).

**Data Processing**

The extended ATR correction was applied for ATR-FTIR spectra. Then data was smoothed (Savitzky-Golay Filter, 11-17 smoothing points, 2nd-3rd polynomial order), baseline was removed (3rd polynomial order), and vector normalization was applied.

The nano-FTIR spectra were baseline corrected (3rd polynomial order), smoothed (Savitzky-Golay Filter, 11 smoothing points, 3rd polynomial order), and normalized (Standard Normal Variate (SNV)). After this procedure, a multivariate data analysis was performed in the range of 1800 $cm^{-1}$ – 1400 $cm^{-1}$.

**Multivariate data analysis**

The Hierarchical Cluster Analysis (HCA) and Principal Component Analysis (PCA) were performed in order to reduce the dimensionality of the data and extract the differences in groups of spectra. The input data consisted of the nanoFTIR spectra of the control group (amyloid-β not treated with bexarotene, incubation time: 4 h), spectra acquired from aggregating (4 h incubation) amyloid-β treated with 10 µM bexarotene, and 100 µM bexarotene. PCA analysis was performed on the second derivatives of the spectra.

**Molecular dynamics (MD)**

The all-atom molecular dynamics (MD) simulations of $A\beta_{(1-42)}$ and bexarotene were performed with the Gromacs 2019.2 package.[4–6] The OPLS-aa force field[7] was used. Sodium and chloride ions were modeled using parameters from Refs.[8] and[9], respectively. The explicit TIP4P model was employed for water.[10] The structure of the $A\beta_{(1-42)}$ was taken from Ref.[11] (Protein Data Bank ID code 2MXU). The topology and input parameters for bexarotene were generated using the LigParGen web server.[12] The NaCl concentration was set to 150 mmol/l. The first step involves single protein simulations, in order to investigate protein-bexarotene interactions. In the second step, to focus on protein-protein interactions in the presence of bexarotene, two protein molecules were used. The ratio of bexarotene to protein molecules was set to 3:1. For both single and multiple protein simulations, the reference systems, i.e., without bexarotene, were calculated. After solvation and ions addition, all the systems were energy minimized, and a 0.2 ns *NVT* equilibration was performed. For single protein systems, ten different initial configurations were simulated in *NPT* ensemble for 400 ns. The systems considering multiple proteins, were simulated in *NPT* ensemble for 150 ns, while for the first 50 ns, the position

restraints were applied on proteins. The first 100 ns of the production run were disregarded in the analysis as the equilibration time.

In all simulations, the Bussi *et al.* stochastic velocity rescaling algorithm[13] was used to control the temperature while the Parrinello–Rahman algorithm was used for the barostat,[14] where the time constants were 0.5 ps and 2 ps, respectively. The temperature and the system pressure were set to 298 K and 1 bar, respectively. The long-range electrostatic interactions were calculated using the PME method,[15] while the van der Waals interactions were described using the Lennard-Jones potential and a 1.0 nm cut-off. LINCS[16] algorithm constrain the bonds between H and heavy atoms in the protein and bexarotene, while for water molecules the SETTLE[17] algorithm was used. A 2 fs time step was used for integrating the equations of motion. VMD software was used for visualizations.[18] The number of H-bonds was calculated using built-in gromacs tools (*gmx hbond*), where the distance and angle cutoffs were 0.35 nm and 30°, respectively.

Classical Ramachandran plot visualizes the energetically allowed regions for protein torsional angles, which provides information on the amino-acid preferences of specific secondary structures.[19] To explore differences in the most occupied regions we proposed a useful approach, i.e., a differential Ramachandran-like plot. It highlights the difference in the probability density of the torsional angle in a given interval. This enables to track small changes in the torsional angle landscapes. Also, slight differences in the probability density, corresponding to changes in the secondary structure content, are exposed.

In this work, the Ramachandran-like plots, showing the probability density of the torsional angles in an interval 1.0° for both angles, were obtained using custom-made script. The distribution of torsional angles ($\phi$ and $\psi$) in $A\beta_{(1-42)}$ protein was determined using built-in Gromacs tools. Positive values on the plot correspond to the increase in the probability density of torsional angles.

**Results and Discussion**

**ATR-FTIR spectroscopy**

**The ATR spectrum of bexarotene**

ATR-FTIR spectrum of bexarotene is presented in Fig. S1. The most prominent peaks of bexarotene are marked: C=O at 1674 $cm^{-1}$, and C-O at 1418 $cm^{-1}$.

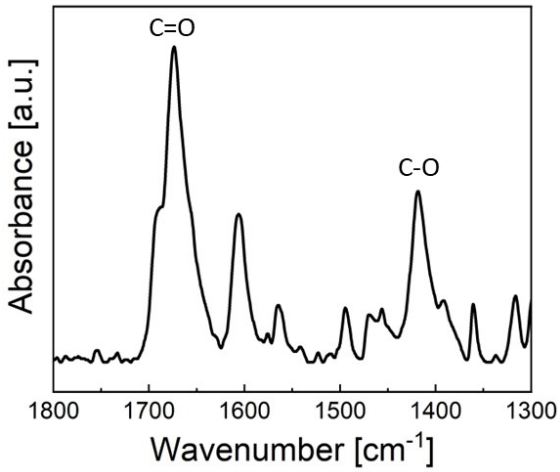


**Fig. S1** ATR-FTIR spectrum of bexarotene.

**ThT kinetics of $A\beta_{(1-42)}$ in the presence and absence of bexarotene**

The time-dependent kinetics of $A\beta_{(1-42)}$ in the presence and absence of bexarotene (Fig. S2) shows that bexarotene inhibits/delays $A\beta_{(1-42)}$ aggregation in a concentration dependent manner. 30 µM $A\beta_{(1-42)}$ in absence of bexarotene, forms amyloid fibrils in 4-5 hours, whereas in presence of 10 µM bexarotene, it takes several hours more time to form fibrils. Higher concentration such as 100 µM delays the aggregation kinetics significantly, which is consistent with our FTIR results. It is interesting to note that bexarotene not only delays/inhibits aggregation rate but also reduces the fibrillar loads. With increasing concentration of bexarotene, lesser amount of $A\beta_{(1-42)}$ fibrils is formed. In presence of 10 molar excess of bexarotene, $A\beta_{(1-42)}$ did not aggregate till 13-15 hours.

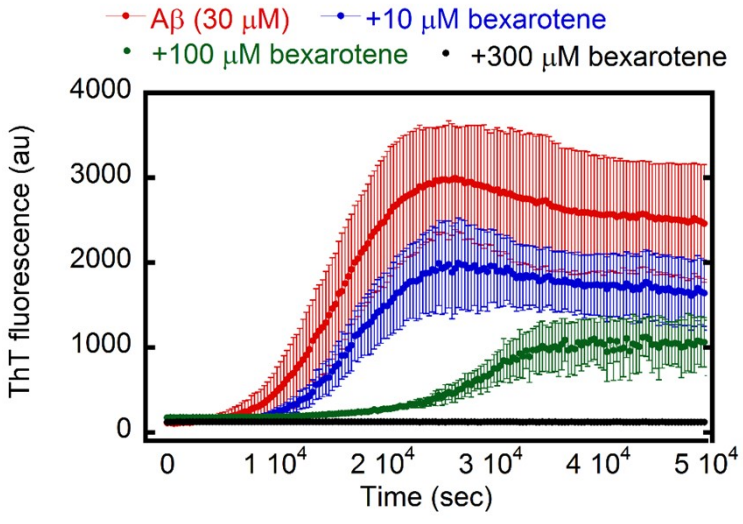


**Fig. S2** The time-dependent kinetics of $A\beta_{(1-42)}$ in the presence and absence of bexarotene.

**Molecular dynamics**

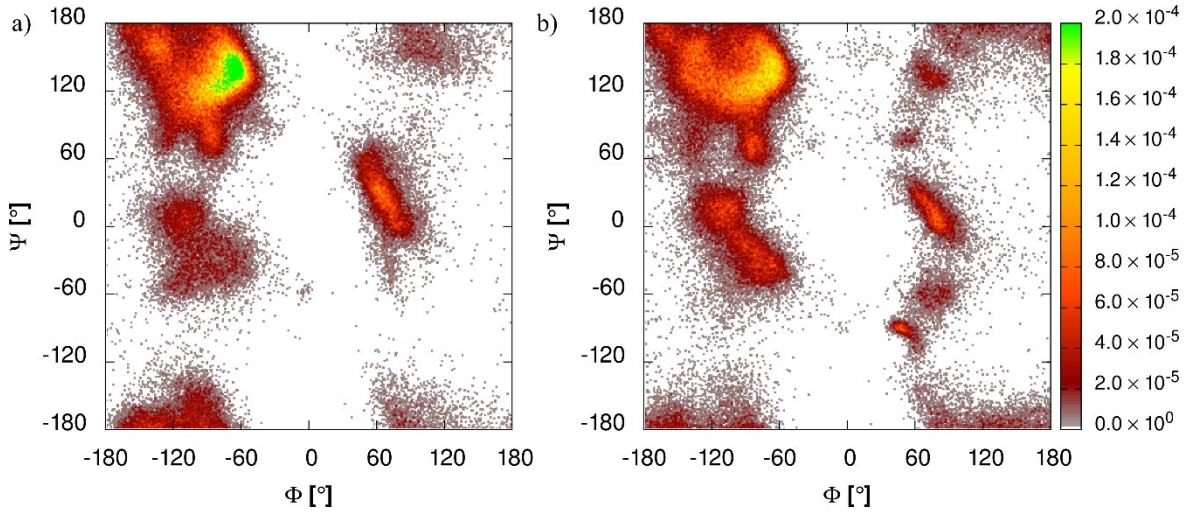


**Fig. S3** The Ramachandran-like diagram of $A\beta_{(1-42)}$ aggregating a) in the absence of bexarotene (reference) and b) in the presence of bexarotene.

**Table S1.** The secondary structure content determined from the MD simulations (average from the last 50 ns), for the reference structure, i.e., without bexarotene (reference), and ten different initial configurations with bexarotene (1-10).

| System | Unstructured | β-sheet & β -bridge | α-helix & 3-helix |
|---|---|---|---|
| Reference | 0.75 | 0.17 | 0.00 |
| 1 | 0.37 | 0.44 | 0.02 |
| 2 | 0.82 | 0.06 | 0.01 |
| 3 | 0.75 | 0.19 | 0.00 |
| 4 | 0.66 | 0.29 | 0.00 |
| 5 | 0.65 | 0.30 | 0.09 |
| 6 | 0.73 | 0.18 | 0.00 |
| 7 | 0.56 | 0.25 | 0.02 |
| 8 | 0.64 | 0.24 | 0.02 |
| 9 | 0.57 | 0.28 | 0.01 |
| 10 | 0.69 | 0.15 | 0.00 |

**References**


1 M. A. Wälti, F. Ravotti, H. Arai, C. G. Glabe, J. S. Wall, A. Böckmann, P. Güntert, B. H. Meier and R. Riek, *Proc. Natl. Acad. Sci. U. S. A.*, 2016, **113**, E4976–E4984.

2 D. Ghosh, M. A. Wälti and R. Riek, in *Methods in Molecular Biology*, Humana Press Inc., 2023, vol. 2551, pp. 41–51.

3 D. Nečas and P. Klapetek, *Open Phys.*, 2012, **10**, 181–188.

4 H. J. C. Berendsen, D. van der Spoel and R. van Drunen, *Comput. Phys. Commun.*, 1995, **91**, 43–56.

5 M. J. Abraham, T. Murtola, R. Schulz, S. Páll, J. C. Smith, B. Hess and E. Lindah, *SoftwareX*, 2015, **1**–**2**, 19–25.

6 S. Pronk, S. Páll, R. Schulz, P. Larsson, P. Bjelkmar, R. Apostolov, M. R. Shirts, J. C. Smith, P. M. Kasson, D. Van Der Spoel, B. Hess and E. Lindahl, *Bioinformatics*, 2013, **29**, 845–854.

7 W. L. Jorgensen and J. Tirado-Rives, *J. Am. Chem. Soc.*, 1988, **110**, 1657–1666.

8 J. Åqvist, *J. Phys. Chem.*, 1990, **94**, 8021–8024.

9 J. Chandrasekhar, D. C. Spellmeyer and W. L. Jorgensen, *J. Am. Chem. Soc.*, 1984, **106**, 903–910.

10 W. L. Jorgensen and J. D. Madura, *Mol. Phys.*, 1985, **56**, 1381–1392.

11 Y. Xiao, B. Ma, D. McElheny, S. Parthasarathy, F. Long, M. Hoshi, R. Nussinov and Y. Ishii, *Nat. Struct. Mol. Biol.*, 2015, **22**, 499–505.

12 L. S. Dodda, I. C. De Vaca, J. Tirado-Rives and W. L. Jorgensen, *Nucleic Acids Res.*, 2017, **45**, W331–W336.

13 G. Bussi, D. Donadio and M. Parrinello, *J. Chem. Phys.*, 2007, **126**, 014101.

14 M. Parrinello and A. Rahman, *J. Appl. Phys.*, 1981, **52**, 7182–7190.

15 U. Essmann, L. Perera, M. L. Berkowitz, T. Darden, H. Lee and L. G. Pedersen, *J. Chem. Phys.*, 1995, **103**, 8577–8593.

16 B. Hess, H. Bekker, H. J. C. Berendsen and J. G. E. M. Fraaije, *J. Comput. Chem.*, 1997, **18**, 1463–1472.

17 S. Miyamoto and P. A. Kollman, *J. Comput. Chem.*, 1992, **13**, 952–962.

18 W. Humphrey, A. Dalke and K. Schulten, *J. Mol. Graph.*, 1996, **14**, 33–38.

19 S. A. Hollingsworth and P. A. Karplus, *Biomol. Concepts*, 2010, **1**, 271–283.